

## Defect physics in 2D monolayer I-VII semiconductor AgI

Ming-Yu Ma <sup>a</sup>, Nian-Ke Chen <sup>a</sup>, Dan Wang <sup>b, \*\*</sup>, Dong Han <sup>c</sup>, Hong-Bo Sun <sup>d</sup>, Shengbai Zhang <sup>e</sup>, Xian-Bin Li <sup>a,\*</sup>



<sup>a</sup> State Key Laboratory of Integrated Optoelectronics, College of Electronic Science and Engineering, Jilin University, Changchun 130012, China

<sup>b</sup> School of Materials Science and Engineering, Beijing Institute of Technology, Beijing 100081, China

<sup>c</sup> State Key Laboratory of Luminescence and Applications, Changchun Institute of Optics Fine Mechanics and Physics, Chinese Academy of Sciences, Changchun 130033, China

<sup>d</sup> State Key Laboratory of Precision Measurement Technology and Instruments, Department of Precision Instrument, Tsinghua University, Beijing 100084, China

<sup>e</sup> Department of Physics, Applied Physics, and Astronomy, Rensselaer Polytechnic Institute, Troy, NY 12180, USA

### ARTICLE INFO

#### Article history:

Received 13 May 2022

Received in revised form

16 December 2022

Accepted 7 January 2023

Available online 13 January 2023

#### Keywords:

Two-dimensional I-VII semiconductor

Monolayer silver iodide

Defect properties

N/p-type doping

First-principles calculations

### ABSTRACT

As a brand new two-dimensional (2D) material with promising electronic properties, monolayer I-VII silver iodide (AgI) has the potential for future 2D electronic devices. To advance the development of such devices, the exploration of *n*-type and *p*-type conductivities of AgI is indispensable. With first-principles calculations, we systematically investigate the properties of intrinsic defects and extrinsic dopants in monolayer AgI, including atomic structural pictures, formation energies, and ionization energies to offer carriers. Considering the divergence in energies of charged defects in 2D materials when the traditional jellium scheme is used, we adopt an extrapolation approach to overcome the problem. The Ag vacancy ( $V_{Ag}$ ) and Be substitution on Ag site ( $Be_{Ag}$ ) are found to be the most promising *p*-type and *n*-type doping candidates, respectively. They could provide bound carriers for transport through the defect-bound band edge states, although the ionization energies are still larger than thermal energy at room temperature. Furthermore, negative-U behaviors are demonstrated in I vacancy ( $V_I$ ), Zn substitution on Ag site ( $Zn_{Ag}$ ), and Cd substitution on Ag site ( $Cd_{Ag}$ ). The present work, for the first time, offers a detailed study of the defect physics in 2D I-VII monolayer semiconductor, laying the foundation for subsequent physics and device explorations based on these brand new 2D materials.

© 2023 Elsevier Ltd. All rights reserved.

## 1. Introduction

While Moore's Law has survived for more than half a century and accurately predicted the stage of technological development [1], it has also become markedly challenging to sustain. The advent of graphene [2] has sparked great interest in 2D materials that are widely recognized candidates to extend Moore's Law. As a representative of Group-IV 2D materials, graphene has unparalleled thermal conductivity and extremely high carrier mobility [3,4]. For Group-V 2D systems, black phosphorus has anisotropic optical properties [5]. Compound semiconductor hexagonal boron nitride, known as the 'ideal substrate' for graphene, is widely used in

electronic devices [6,7]. In the family of 2D II-VI materials, monolayer BeO is predicted by first-principles calculations to have good stability and has been synthesized in the experiment [8–10]. Possessing high electron mobility and anomalous optical response, InSe, an exemplar III-VI semiconductor, is conducive to the development of ultrathin electronic devices [11,12]. Another III-VI semiconductor, In<sub>2</sub>Se<sub>3</sub>, is reported to be an excellent material for ferroelectric memory [13–15]. Transition metal dichalcogenides such as MoS<sub>2</sub> enjoy indirect-to-direct band gap transition when the thickness is reduced to a monolayer [16]. It is worthwhile to note that the defect physics studies of the above material groups have been thoroughly carried out for their device developments [17–22].

Group I-VII materials form another important type of semiconductor family. Among them, the silver iodide (AgI) in its three-dimensional (3D) structures usually has the direct band gap [23–25], being promising in device applications [26]. Its 2D AgI counterpart, with the advantage of strong ionicity, has been very recently predicted to have a dynamically stable structure even at its

\* Corresponding author.

\*\* Corresponding author.

E-mail addresses: [dan.wang@bit.edu.cn](mailto:dan.wang@bit.edu.cn) (D. Wang), [lixianbin@jlu.edu.cn](mailto:lixianbin@jlu.edu.cn) (X.-B. Li).

monolayer form [27]. This opens the door for the community to consider using this new kind of 2D material. To be applied in electronic devices, the defect properties of such new material, particularly an achievable and sustaining *p/n*-type conductivity, are imperative [28]. However, to the best of our knowledge, studies on the defect behavior of Group I-VII 2D semiconductors have not been witnessed previously.

In this work, we systematically studied stable structures, formation energies, and converged ionization energies of intrinsic defects and substitutional impurities in monolayer I-VII AgI by first-principles calculations and the WLZ extrapolation method for charged defects in 2D materials [18,19]. The possible *n*-type and *p*-type doping candidates are explored. The studied intrinsic defects include Ag vacancy ( $V_{\text{Ag}}$ ) and I vacancy ( $V_{\text{I}}$ ). The substitutional defects include Group VI-A elements on I site ( $\text{S}_{\text{I}}$ ,  $\text{Se}_{\text{I}}$ ,  $\text{Te}_{\text{I}}$ ), Group II-B elements on Ag site ( $\text{Zn}_{\text{Ag}}$ ,  $\text{Cd}_{\text{Ag}}$ ,  $\text{Hg}_{\text{Ag}}$ ), and Group II-A elements on Ag site ( $\text{Be}_{\text{Ag}}$ ,  $\text{Mg}_{\text{Ag}}$ ,  $\text{Ca}_{\text{Ag}}$ ,  $\text{Sr}_{\text{Ag}}$ , and  $\text{Ba}_{\text{Ag}}$ ). We find that  $V_{\text{Ag}}$  and  $X_{\text{I}}$  ( $X = \text{S}, \text{Se}$ , and  $\text{Te}$ ) are acceptors, whereas  $X_{\text{Ag}}$  ( $X = \text{Be}, \text{Mg}, \text{Ca}, \text{Sr}, \text{Ba}$ ) are donors. However,  $\text{Hg}_{\text{Ag}}$  has both deep donor and acceptor transition levels. Among all the defects,  $\text{Be}_{\text{Ag}}$  and  $V_{\text{Ag}}$  are the shallowest donor and acceptor respectively, with ionization energies being 0.26 eV and 0.432 eV, respectively. They are still larger than the thermal energy at room temperature. However, they may contribute to considerable *n*-type and *p*-type conductivities through the defect-bound band edge (DBBE) states [22]. For  $V_{\text{I}}$ ,  $\text{Zn}_{\text{Ag}}$ , and  $\text{Cd}_{\text{Ag}}$ , they tend to behave as negative-U defects with the (+1/0) donor transition level above the (0/-1) acceptor transition level, which can be ascribed to the high sensitivity of the atomic configuration to the charged states.

## 2. Computational methods

We perform first-principles calculations based on density functional theory (DFT) in the VASP codes [29,30]. Projector augmented-wave basis and generalized gradient approximation (GGA) with the Perdew–Burke–Ernzerhof (PBE) [31] functional are employed. Ag (4d<sup>10</sup> and 5s<sup>1</sup>) and I (5s<sup>2</sup> and 5p<sup>5</sup>) electrons are treated as valence electrons in the pseudopotential [32]. The cutoff energy of the plane wave base is 260 eV for perfect AgI and defective systems with dopants (including  $\text{Be}_{\text{Ag}}$ ,  $\text{Mg}_{\text{Ag}}$ ,  $\text{Ca}_{\text{Ag}}$ ,  $\text{Sr}_{\text{Ag}}$ ,  $\text{Ba}_{\text{Ag}}$ ,  $\text{Se}_{\text{I}}$ , and  $\text{Te}_{\text{I}}$ ) and 300 eV for defective systems with dopants (including  $\text{S}_{\text{I}}$ ,  $\text{Zn}_{\text{Ag}}$ ,  $\text{Cd}_{\text{Ag}}$ , and  $\text{Hg}_{\text{Ag}}$ ). A 16 × 16 × 1 Monkhorst-Pack mesh grid is used for the k-point sampling for unit cell calculations and 1 × 1 × 1 for supercell calculations. In the NVT *ab initio* molecular dynamics simulations (AIMD) [33], the temperature is risen linearly from 0 K to 400 K for 2 ps and is kept at 400 K for 20 ps with a time step of 1 femtosecond. The effects of spin polarization are all included in all the calculations. All atoms are relaxed until the Hellmann–Feynman forces on individual atoms are less than 0.02 eV Å<sup>-1</sup>. The phonon spectrum of the monolayer AgI is calculated by the Phonopy code [34]. The vdW interactions of two layers structures are considered using the DFT-D3 method [35].

The formation energy for one defect  $w$  with charge  $q$  is defined as [36,37].

$$\Delta H_f(q, w) = E_{\text{tot}}(q, w) - E_{\text{tot}}(\text{host}) + \sum_i n_i(E_i + \mu_i) + q(\varepsilon_{\text{VBM}} + \varepsilon_F) \quad (1)$$

where  $E_{\text{tot}}(q, w)$  is the total energy of the supercell containing the defect  $w$  with charged quantity  $q$ , and  $E_{\text{tot}}(\text{host})$  is the energy of the same-size supercell without defects.  $i$  stands for the element.  $n_i$  is the number of atoms exchanged for every element during the defect formation.  $E_i$  is the chemical potential when it exists in the form of the most stable state at normal temperature and pressure,

and  $\mu_i$  is the relative chemical potential of the element, reflecting the influence of different experimental conditions on the formation energy. Under thermal equilibrium, the chemical potential of host atoms must satisfy:  $\mu_I + \mu_{\text{Ag}} = \Delta H(\text{AgI})$ . Here,  $\Delta H(\text{AgI})$  is the formation enthalpy of the monolayer AgI.  $\varepsilon_{\text{VBM}}$  equalizes the energy position of the valence band maximum (VBM) of the perfect host system, and  $\varepsilon_F$  is the Fermi energy relative to the  $\varepsilon_{\text{VBM}}$ .

It can be seen from Eq. (1) that the formation energy of charged defects depends on the electron Fermi level  $\varepsilon_F$ . The Fermi level when a defect has the same formation energy in different charged states (such as  $q$  and  $q'$ ) is called the transition level  $\varepsilon(q/q')$ , where  $q$  and  $q'$  are two charged states of the same defect.

$$\varepsilon(q/q') + \varepsilon_{\text{VBM}} = [E_{\text{tot}}(q, w) - E_{\text{tot}}(q', w)] / (q' - q) \quad (2)$$

The ionization energy (*IE*) of the defect can be defined by the transition energy level (from  $q = +1$  to  $q = 0$  for a donor and from  $q = 0$  to  $q = -1$  for an acceptor). The ionization energy is the energy required to ionize the electrons or holes of the impurity to the corresponding energy band edges to become free carriers. In the meanwhile, *IE* is the most important physical quantity to measure the defect performance. That is:

$$\begin{aligned} \text{IE(donor)} &= \varepsilon_{\text{CBM}} \\ &- \varepsilon(+1/0) \text{ and } \text{IE(acceptor)} = \varepsilon(0/-1) - \varepsilon_{\text{VBM}} \end{aligned} \quad (3)$$

Here,  $\varepsilon_{\text{CBM}}$  equalizes the energy position of the conduction band minimum (CBM). Due to the long-range Coulomb interaction of the charged defect with its periodic images and the compensating jellium charges, the charged formation energy and ionization energy of defects in 2D materials are divergent [19,38]. Here, to get the converged ionization energy, we follow the WLZ extrapolation method developed in our previous work [19]. This is a key step to evaluate the defect physics in 2D materials.

$$\text{IE}(S, L_Z) = \text{IE}_0 + \frac{\alpha}{\sqrt{S}} + \beta \frac{L_Z}{S} \quad (4)$$

where  $\text{IE}(S, L_Z)$  is the size-dependent ionization energy,  $\text{IE}_0$  is the true, size-independent ionization energy.  $S$  and  $L_Z$  are lateral size and vacuum size of the calculated supercell, respectively.  $\alpha$  is the defect-specific Madelung constant and  $\beta = e^2/(24\varepsilon_0)$ . The  $\text{IE}_0$  is obtained by extrapolating Eq. (4) with supercell sizes varying from lateral 5 × 5 to 7 × 7 for  $L_X \times L_Y$ , with the vacuum of 20 Å to 40 Å for  $L_Z$ .

## 3. Results and discussions

The relaxed structure of monolayer AgI at 0 K is shown in Fig. 1(a). It consists of two buckled honeycomb atomic layers [27]. The lattice constant is 4.562 Å, which coincides with the experimental lattice parameter in the (111) hexagonal plane of zincblende AgI, 4.591 Å [39]. The in-plane and out-of-plane Ag–I bond lengths are both 2.91 Å at 0 K. We calculated the phonon spectrum of the monolayer AgI, as shown in Fig. 1(b). The three acoustic modes show no obvious imaginary frequency, which is consistent with previous study [27] and demonstrates the dynamic stability of the monolayer AgI. Fig. 1(c) presents its projected electronic band structure. It has a direct GGA band gap of 2.08 eV at  $\Gamma$  point, retaining the character of the direct band gap of its 3D bulk form [24,25]. The partial density of states (PDOS) as shown in Fig. 1(d) reveals that the lowest conduction band is dominated by the p orbitals of I atoms and s orbital of Ag atoms, and the highest valence band is mainly contributed by the p orbitals of I atoms and d orbital of Ag atoms. As shown in Fig. 1(e), the in-plane bond length has

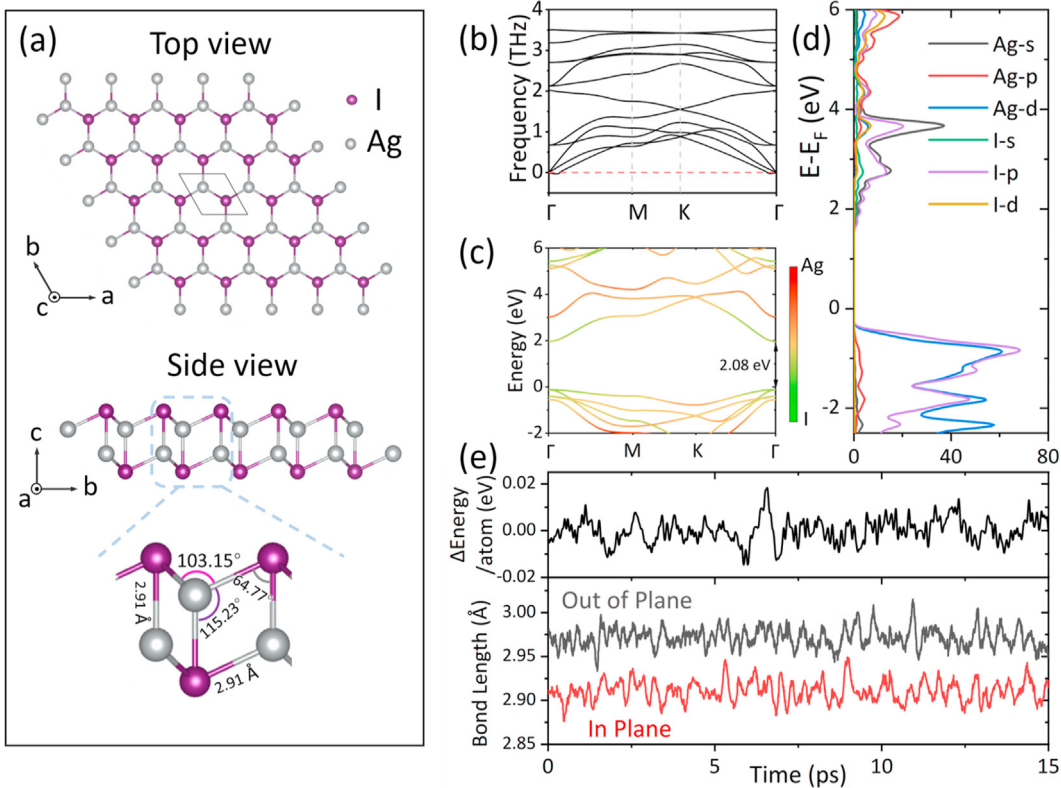


**Fig. 1.** (a) Top view and side view of the relaxed structure of the monolayer AgI. (b) The corresponding calculated phonon spectrum of the monolayer AgI. (c) Projected electronic band structure with red and green indicating weights of Ag and I atomic orbital projections. (d) Partial density of states (PDOS) of the monolayer AgI. (e) Evolution of average bond length (Out of Plane, In Plane) and energy averaged per atom of the monolayer AgI in a 400-K AIMD simulation. (For interpretation of the references to color in this figure legend, the reader is referred to the Web version of this article.)

little changed and the out-of-plane one increases slightly by 2% in a 400-K molecular dynamics simulation. The results are obtained from the last 15 ps of the 20 ps MD simulation.  $\Delta\text{Energy}/\text{atom}$  is energy averaged per atom with a reference to the averaged value during the MD at 400 K. The small variation in bond length and energy shows the monolayer AgI has good thermal stability.

For materials used in the application of electronics and optoelectronics, a systematic understanding of defects or doping properties, particularly the ability to supply carriers, is very essential. For the monolayer AgI, we investigated the formation energy and ionization energy of four kinds of defects in three different charged states [(1-), (0), and (1+)], including intrinsic defects (I vacancy,  $V_I$  and Ag vacancy,  $V_{\text{Ag}}$ ), Group VI-A substitutional impurities on I site ( $S_I$ ,  $Se_I$ ,  $Te_I$ ), Group II-B substitutional impurities on Ag site ( $Zn_{\text{Ag}}$ ,  $Cd_{\text{Ag}}$ ,  $Hg_{\text{Ag}}$ ), and Group II-A substitutional impurities on Ag site ( $Be_{\text{Ag}}$ ,  $Mg_{\text{Ag}}$ ,  $Ca_{\text{Ag}}$ ,  $Sr_{\text{Ag}}$ ,  $Ba_{\text{Ag}}$ ). The calculated local atomic structures of all the defects in their neutral states are shown in Fig. 2.

Using the WLZ extrapolation approach described in the section of Methods, we obtained the converged ionization energies and formation energies of these defects, as shown in Fig. 3. The formation energies are calculated under both the Ag-rich/-poor conditions with avoiding the formation of secondary phases related to the dopants [36,37]. Here, the secondary phases including  $Ag_2S$ ,  $Ag_2Se$ ,  $Ag_2Te$ ,  $ZnI_2$ ,  $CdI_2$ ,  $HgI_2$ ,  $BeI_2$ ,  $MgI_2$ ,  $CaI_2$ ,  $SrI_2$ ,  $BaI_2$  [40] are considered for various substitutional dopants respectively. Also, the relative chemical potential of a dopant should be also not larger than zero to circumvent the formation of the elementary substance of the dopant. It can be seen in Fig. 3(a), (b) that the formation energy of  $V_I$  under the Ag-rich condition is lower than that under the Ag-poor condition, while the formation energy of  $V_{\text{Ag}}$  under the

Ag-poor condition is lower than that under the Ag-rich condition. This is easily understandable that the low iodide concentration under the Ag-rich condition promotes the formation of  $V_I$  and vice versa under the Ag-poor condition. However, at a first glance, it seems to be strange that  $X_{\text{Ag}}$  ( $X = Zn$ ,  $Cd$ ,  $Hg$ ,  $Be$ ,  $Mg$ ,  $Ca$ ,  $Sr$ , and  $Ba$ ) dopants have higher formation energies at the Ag-poor condition than those at the Ag-rich condition, in Fig. 3(e)–(h). This is due to the consideration of avoiding the formation of secondary phases of dopants with host elements. The formation energies of  $X_I$  ( $X = S$ ,  $Se$ , and  $Te$ ) at the Ag-rich and Ag-poor conditions are also analyzed in the same way, as shown in Fig. 3(c), (d). Overall, the range of formation energies discussed above reflects a reasonable possibility of the formation of these defects.

Fig. 4 summarizes the transition levels (and ionization energies) of all the studied defects. For  $V_I$ ,  $Zn_{\text{Ag}}$ , and  $Cd_{\text{Ag}}$ , the stable states are found to be only (+1) and (-1) when the Fermi level is within the band gap, with the (+1/-1) transition levels being 0.968 eV, 1.214 eV, 1.105 eV above the VBM, respectively. This implies that the transition level of (0/-1) is below the level of (+1/0) for the three defect systems and thus  $V_I$ ,  $Zn_{\text{Ag}}$ , and  $Cd_{\text{Ag}}$  are all negative-U defects [41]. The origin of the negative-U defect will be discussed later.  $V_{\text{Ag}}$  is a typical acceptor-type defect with the corresponding (0/-1) transition level located at 0.432 eV above the VBM. Since the Group VI-A elements ( $S$ ,  $Se$ ,  $Te$ )/Group II-A elements ( $Be$ ,  $Mg$ ,  $Ca$ ,  $Sr$ , and  $Ba$ ) have one less/more electron than  $I/\text{Ag}$ ,  $X_I$  ( $S_I$ ,  $Se_I$ ,  $Te_I$ ) and  $X_{\text{Ag}}$  ( $Be_{\text{Ag}}$ ,  $Mg_{\text{Ag}}$ ,  $Ca_{\text{Ag}}$ ,  $Sr_{\text{Ag}}$ ,  $Ba_{\text{Ag}}$ ) are favorable acceptor-type and donor-type defects, respectively. The (0/-1) transition level of  $S_I$ ,  $Se_I$ , and  $Te_I$  are 0.7 eV, 0.761 eV, and 0.827 eV above VBM, while the (+1/0) transition level of  $Be_{\text{Ag}}$ ,  $Mg_{\text{Ag}}$ ,  $Ca_{\text{Ag}}$ ,  $Sr_{\text{Ag}}$ , and  $Ba_{\text{Ag}}$  are 0.26 eV, 0.283 eV, 0.26 eV, 0.273 eV, and 0.292 eV under CBM. For  $Hg_{\text{Ag}}$ , the stable states are found to be (+1), (0), and (-1) when the Fermi

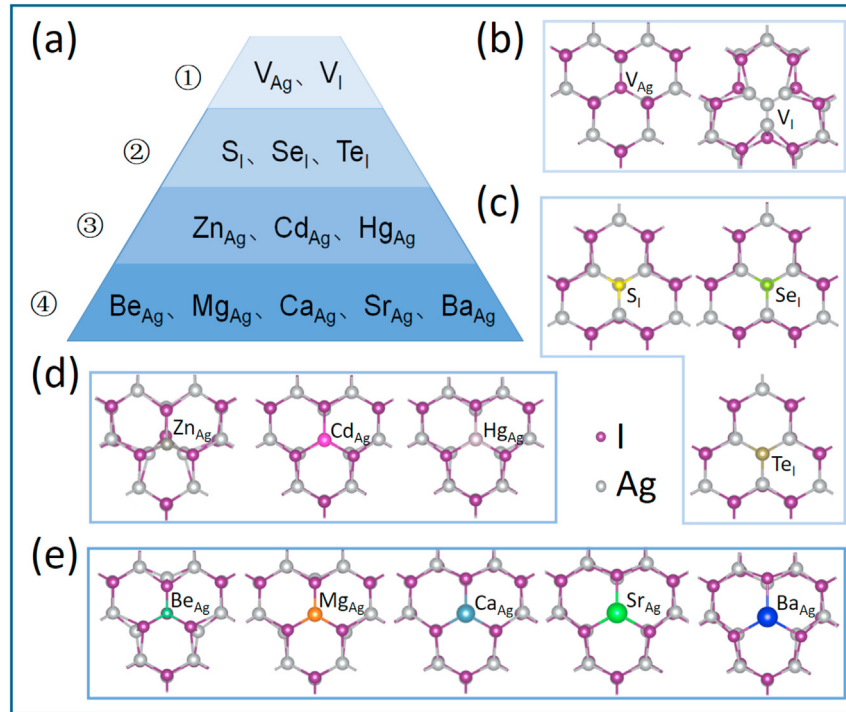


**Fig. 2.** (a) Classification of the calculated defects. The relaxed local structures in the neutral states of the (b) intrinsic defects, (c) three Group VI-A substitutional defects on I site, (d) three Group II-B substitutional defects on Ag site, and (e) five Group II-A substitutional defects on Ag site.

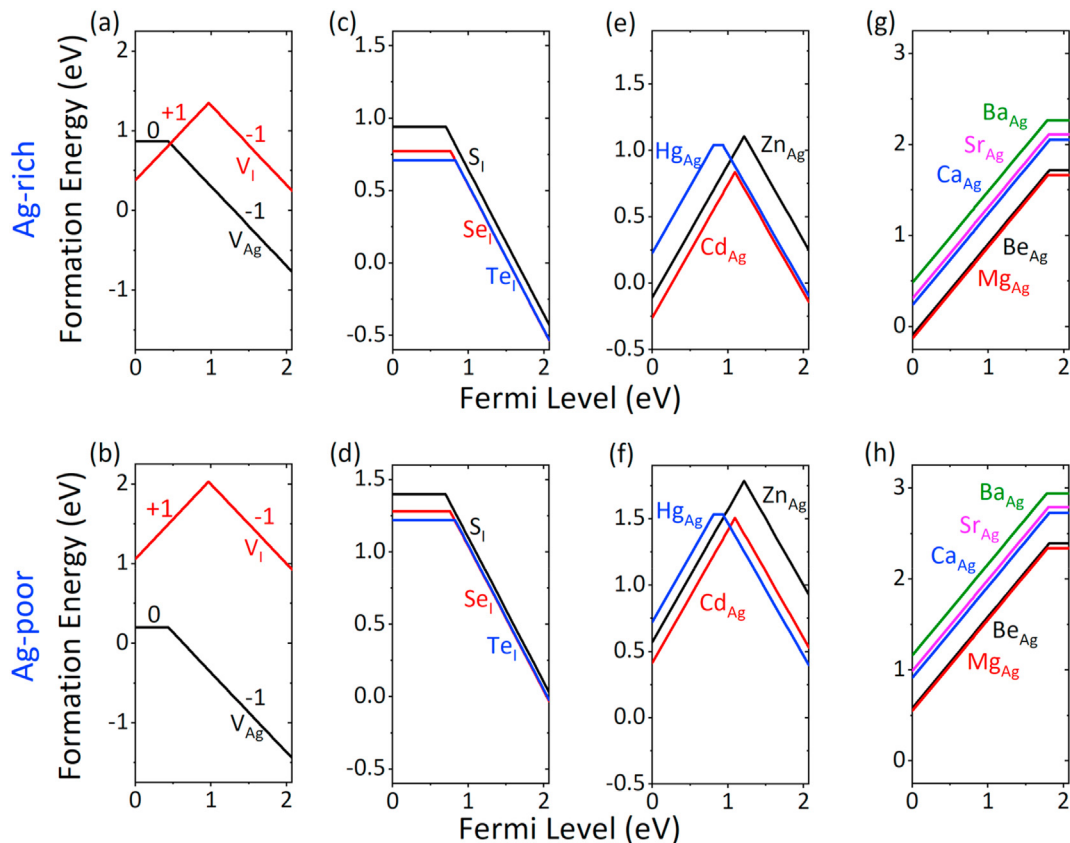


**Fig. 3.** The formation energy of the native and substitutional defects as a function of the Fermi level. (a) and (b) show the results of  $V_I$  and  $V_{Ag}$ . (c)–(h) show the results of Ag-substituted and I-substituted defects. The top and bottom figures account for the Ag-rich and Ag-poor conditions, respectively. The Fermi level varies from 0 at the VBM to 2.08 eV at the CBM of monolayer AgI.

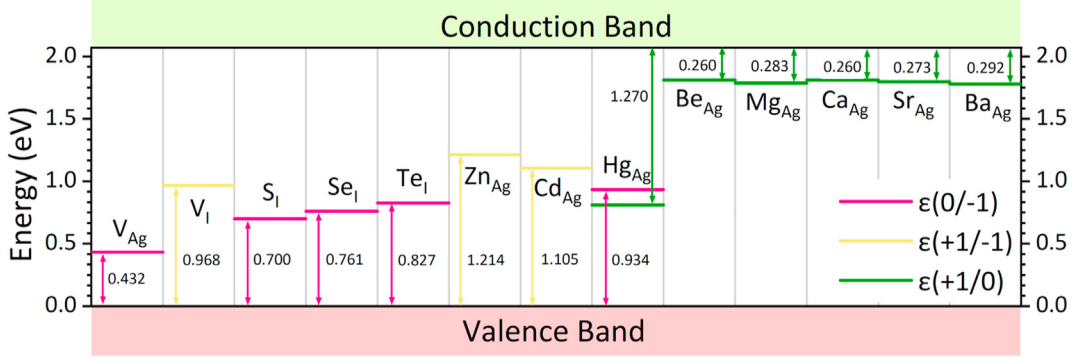


**Fig. 4.** The summary of transition levels and ionization energies of all the calculated defects in the monolayer AgI. The red, yellow, and green lines stand for the  $(0/-1)$ ,  $(+1/-1)$ , and  $(+1/0)$  transition levels, respectively. The corresponding values of ionization energies for the defects are also noted. (For interpretation of the references to color in this figure legend, the reader is referred to the Web version of this article.)

level spans from VBM to CBM. The  $(0/-1)$  transition level is 0.934 eV above VBM and the  $(+1/0)$  transition level is 1.270 eV under CBM. Among all the defects in this work,  $V_{Ag}$  is the shallowest acceptor, whereas the shallowest donor is  $Be_{Ag}$ , meaning that they can be more easily ionized than other acceptor/donor defects. Note that  $Be_{Ag}$  has a lower formation energy than that of  $Ca_{Ag}$ , whose ionization energy is also 0.26 eV. That reflects  $Be_{Ag}$  is a more easily formed donor defect.

Though the ionization energy of 0.26 eV of  $Be_{Ag}$  is larger than the thermal energy at room temperature,  $Be_{Ag}$  is still promising to provide carriers for effective transport given the unique ionization picture of defects in 2D materials [22]. Due to the weak screening of 2D materials, the ionized carriers are bound by the charged defect after being excited to the band edge. Thus, the ionization energy consists of the energy for carrier excitation and the binding energy between the carrier and the charged defect. The former should be negligible for  $Be_{Ag}$  according to the band structure as shown in Fig. 5(a). The defect state (red line) is above the lowest conduction band, meaning a spontaneous falling of the extra electron of Be from the defect state to the conduction band edge. We also calculated the band structure of  $Be_{Ag}$  using HSE06 [42], which shows the similar picture of the defect states above the

lowest conduction band as PBE does. This reveals that the binding energy of the positively charged Be ion with the electron equals 0.26 eV. The conduction band edge occupied by the bound electron is called defect-bound band edge (DBBE) states and can be a platform for carrier transport via wavefunction overlap at a reasonable doping density [22]. Moreover, an increase in the screening by such as adding a substrate will further enhance the overlap and thus the carrier transport [43–45]. We demonstrate the substrate screening effect by putting another perfect AgI layer under the defective AgI layer and calculating the converged ionization energy of  $Be_{Ag}$ , which is 0.20 eV. This is ascribed to increased screening induced by the perfect AgI layer. The atoms are not allowed to relax for computational efficiency after we put the two layers together.

In contrast, for the deep defects with defect states within the band gap, such as  $Te_I$  [one typical example of the Group-VIA element replacing iodine site], of which the band structures are shown in Fig. 5(b), (c), the energy required for exciting the hole from the defect state in the spin-down channel to the valence band edge is considerable. This means that as an acceptor,  $Te_I$  hardly donates a hole for transport. Other doping techniques such as

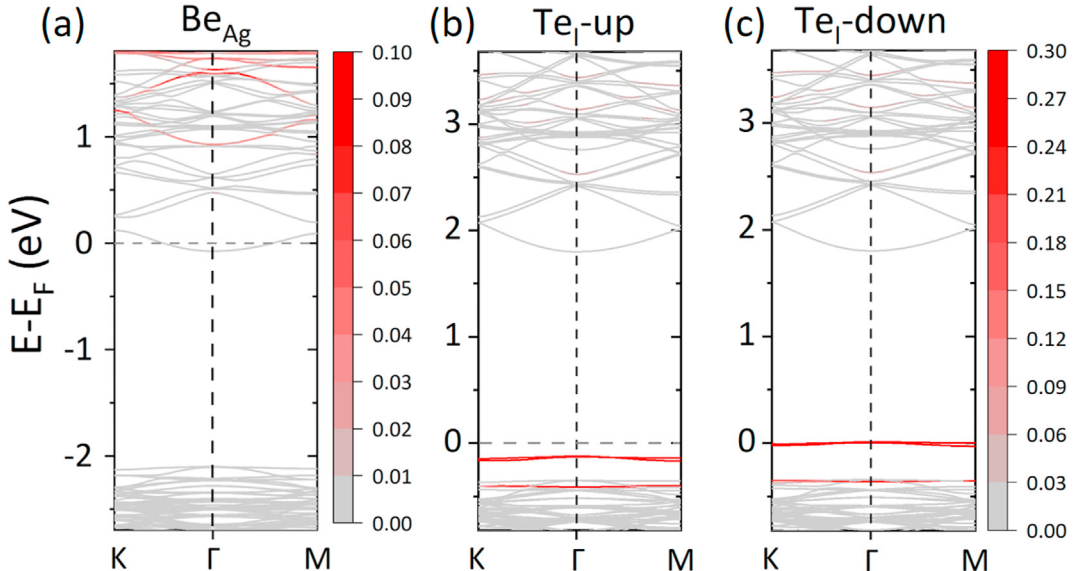


**Fig. 5.** Band structure of AgI with: (a)  $Be_{Ag}$ ; (b) spin-up part and (c) spin-down part for  $Te_I$  in their neutral states. The projected contribution of the defect atom to the energy band is displayed according to the intensity color bars. (For interpretation of the references to color in this figure legend, the reader is referred to the Web version of this article.)

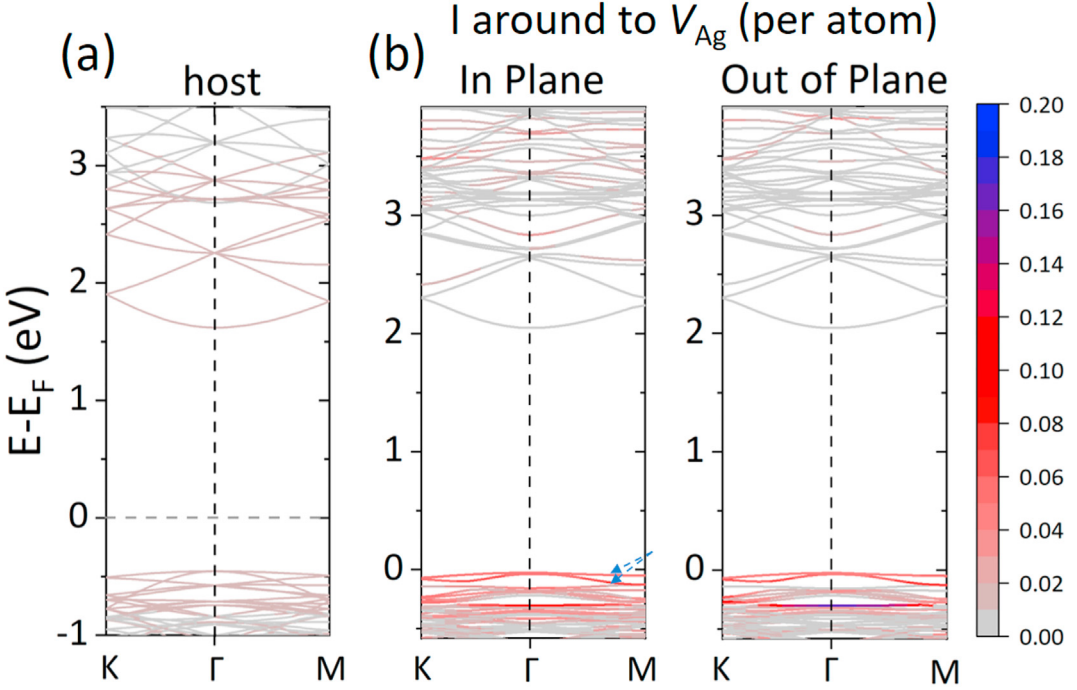


**Fig. 6.** Band structure: (a) undoped AgI in supercell; (b) AgI supercell with a V<sub>Ag</sub>. The projected contribution of I atom around the V<sub>Ag</sub> to the energy band is shown according to the intensity color bar. For V<sub>Ag</sub>, the neighboring I atoms include three in-plane ones (the averaged value per I atom is shown) and an out-of-plane one. For comparison, the projected contribution of the I atom (the averaged value per I atom) in the perfect monolayer AgI is also shown in (a). The occupation probability at  $\Gamma$  of the two upmost valence bands denoted by the blue arrows in (b) is not full (0.6–0.7), indicating a spontaneous hole doping at VBM for V<sub>Ag</sub>. (For interpretation of the references to color in this figure legend, the reader is referred to the Web version of this article.)

modulation doping [46] and molecular doping [47] have also been proposed for achievable n-type/p-type doping of 2D materials. In recent years, to speed up the calculation efficiency of defect-related and other properties of 2D materials, machine learning techniques have been applied [48,49].

The DBBE state is also found in V<sub>Ag</sub>, as shown in Fig. 6. Compared to the band structure of the perfect AgI, the creation of Ag vacancy leads to a partially occupied highest valence band and induces no defect states within the band gap, indicating that the highest valence band accepts a hole from the defect state below the VBM

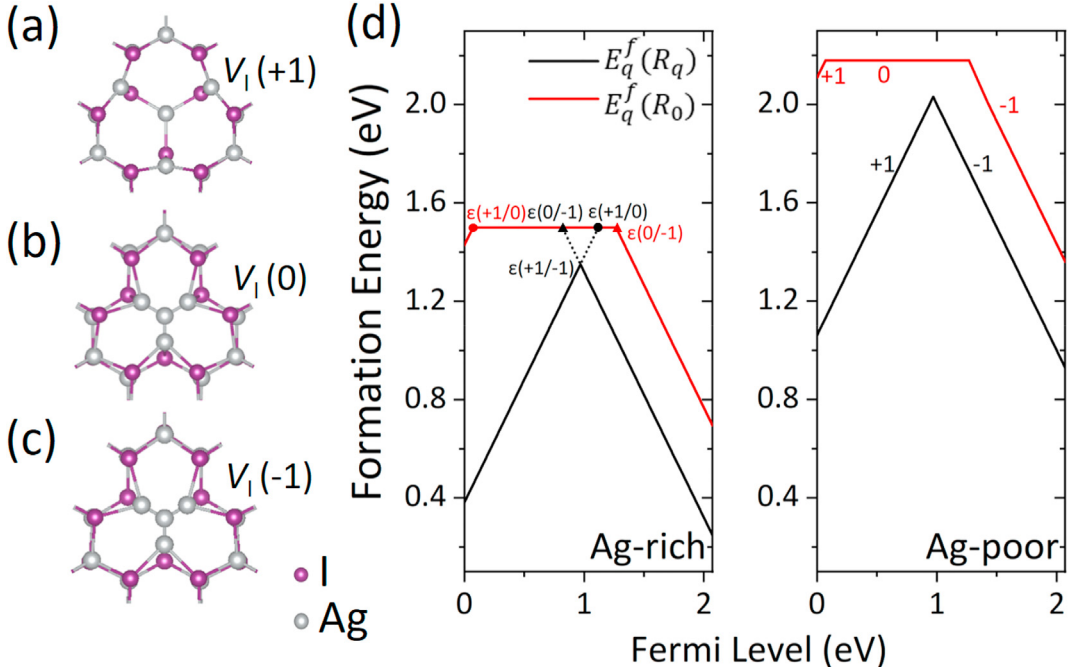


**Fig. 7.** (a)–(c) The relaxed structure of V<sub>1</sub> in different charged states. (d) The formation energy of V<sub>1</sub> with charged state of  $q$  and relaxed geometry  $R_q$  at the Ag-rich/Ag-poor conditions. The circles and triangles stand for the transition level of (+1/0) and (0/-1), respectively. The black/red color stands for the transition levels obtained with the structure of  $R_q/R_0$ . (For interpretation of the references to color in this figure legend, the reader is referred to the Web version of this article.)

with no energy cost. Like the discussion of the DBBE state above, the hole at the highest valence band edge should be bound by the negatively charged  $V_{Ag}$  and the binding energy between them is equivalent to the ionization energy of  $V_{Ag}$ , i.e., 0.432 eV. In terms of the magnitude of the binding energy,  $V_{Ag}$  in monolayer AgI is comparable to the  $Re_{Mo}$  in monolayer MoS<sub>2</sub>, which could be the origin of the spontaneous n-type conductivity of MoS<sub>2</sub> [22]. Therefore, it can speculate that  $V_{Ag}$  in monolayer AgI is likely to provide p-type conductivity.

Finally, we investigated the origin of the negative-U behavior in  $V_I$ , Cd<sub>Ag</sub>, and Zn<sub>Ag</sub>. Here, we take  $V_I$  as an example. Fig. 7(a)–(c) show the relaxed equilibrium atomic structure of  $V_I$ , which is denoted by  $R_q$ , where  $q$  is the charged state ( $q = +1, 0$ , and  $-1$ ) and Fig. 7(d) presents the formation energy of  $V_I$ , which is labeled as  $E_f^f(R_q)$ . The significant variation between  $R_0$  and  $R_{+1}$  corroborates with the large energy reduction from  $E_{+1}^f(R_0)$  to  $E_{+1}^f(R_{+1})$ , greatly moving the transition level of (+1/0) towards CBM by 1.047 eV, from the red-circle position to the black-circle position as shown in Fig. 7(d). On the contrary, for the charge state of  $q = -1$ , the minor change between  $R_0$  and  $R_{-1}$  results in a small energy reduction from  $E_{-1}^f(R_0)$  to  $E_{-1}^f(R_{-1})$  and a slight movement of the transition level of (0/-1) towards VBM by 0.447 eV, from the red-triangle position to black-triangle position in Fig. 7(d). The much larger shift of transition level of (+1/0) than the one of (0/-1) eventually makes their positions inverted from the usual order and thus leads to the negative-U behavior. We stress that  $V_I$  is still a deep defect although the negative-U behavior makes it shallower than the case with the zero charged structure ( $R_0$ ).

#### 4. Conclusion

In summary, we comprehensively studied the defect properties of intrinsic vacancies and substitutional dopants in monolayer I-VII semiconductor, AgI by *ab initio* calculations. The WLZ extrapolation method is adopted to converge the charged formation energy and ionization energy of the defects. The  $X_{Ag}$  ( $X = Be, Mg, Ca, Sr, Ba$ ) are shallow donors, with the ionization energies in a range of 0.26–0.292 eV, and  $X_I$  ( $X = S, Se, Te$ ) are deep acceptors, with the ionization energies in a range of 0.7–0.827 eV. For  $X_{Ag}$  ( $X = Zn, Cd$ , and Hg), they have both deep donor and acceptor transition levels. The shallowest donor is  $Be_{Ag}$  with an ionization energy of 0.26 eV while the shallowest acceptor is  $V_{Ag}$  with an ionization energy of 0.432 eV. For  $Be_{Ag}$  and  $V_{Ag}$ , the electron and hole may transport through the defect bound CBM and VBM, respectively, making them promising carriers to contribute to the n-type and p-type conductivities of monolayer AgI. Furthermore, we found that  $V_I$ , Zn<sub>Ag</sub>, and Cd<sub>Ag</sub> are negative-U defects since their structure is highly sensitive to the charged states. Most recently, note that 2D AgI has been successfully synthesized in experiments [50–52], making the defect study of 2D I-VII materials imperative since doping is the essential element for such materials to be used in electronic/optoelectronic devices. It is the first time that the defect properties of 2D I-VII semiconductor materials are carefully analyzed, which paves the way for subsequent physics exploration and device application based on such brand-new 2D materials.

#### Credit author statement :

**Ming-Yu Ma:** Formal analysis, Investigation, Writing - Original Draft. **Nian-Ke Chen:** Software, Supervision. **Dan Wang:** Methodology, Investigation, Writing - Review & Editing, Supervision. **Dong Han:** Supervision. **Hong-Bo Sun:** Supervision. **Shengbai Zhang:** Supervision. **Xian-Bin Li:** Conceptualization, Project administration, Writing - Review & Editing, Supervision.

#### Declaration of competing interest

- (1) All authors disclosed no relevant relationships.
- (2) The author(s) declared no potential conflicts of interest with respect to the research, authorship, and/or publication of this article.

#### Data availability

Data will be made available on reasonable request.

#### Acknowledgments

Work in China was supported by the National Natural Science Foundation of China (Grants Nos. 11874171, 11904118, 11974344, 61922035, 12274172), the Fundamental Research Funds for the Central Universities, and China Postdoctoral Science Foundation (2019M661200) and the Open Fund of the State Key Laboratory of Integrated Optoelectronics (Grant No. IOSKL2020KF07). Work at RPI was supported by the US Department of Energy under Grant No. DE-SC0002623. We also acknowledge the High-Performance Computing Center (HPCC) at Jilin University for calculation resources.

#### References

- [1] G.E. Moore, Cramming more components onto integrated circuits, *Electro-Magnetobiol.* 38 (1965) 114–117, <https://doi.org/10.1109/jproc.1998.658762>.
- [2] K.S. Novoselov, A.K. Geim, S.V. Morozov, D. Jiang, Y. Zhang, S.V. Dubonos, I.V. Grigorieva, A.A. Firsov, Electric field effect in atomically thin carbon films, *Science* 306 (2004) 666–669, <https://doi.org/10.1126/science.1102896>.
- [3] K.S. Novoselov, A.K. Geim, S.V. Morozov, D. Jiang, M.I. Katsnelson, I.V. Grigorieva, S.V. Dubonos, A.A. Firsov, Two-dimensional gas of massless Dirac fermions in graphene, *Nature* 438 (2005) 197–200, <https://doi.org/10.1038/nature04233>.
- [4] A.A. Balandin, S. Ghosh, W. Bao, I. Calizo, D. Teweldebrhan, F. Miao, C.N. Lau, Superior thermal conductivity of single-layer graphene, *Nano Lett.* 8 (2008) 902–907, <https://doi.org/10.1021/nl0731872>.
- [5] J. Qiao, X. Kong, Z.-X. Hu, F. Yang, W. Ji, High-mobility transport anisotropy and linear dichroism in few-layer black phosphorus, *Nat. Commun.* 5 (2014) 4475, <https://doi.org/10.1038/ncomms5475>.
- [6] C.R. Dean, A.F. Young, I. Meric, C. Lee, L. Wang, S. Sorgenfrei, K. Watanabe, T. Taniguchi, P. Kim, K.L. Shepard, J. Hone, Boron nitride substrates for high-quality graphene electronics, *Nat. Nanotechnol.* 5 (2010) 722–726, <https://doi.org/10.1038/nano.2010.172>.
- [7] X.-D. Li, N.-K. Chen, B.-Q. Wang, X.-B. Li, Conductive mechanism in memristor at the thinnest limit: the case based on monolayer boron nitride, *Appl. Phys. Lett.* 121 (2022), 073505, <https://doi.org/10.1063/5.0098120>.
- [8] H. Zhang, M. Holbrook, F. Cheng, H. Nam, M. Liu, C.-R. Pan, D. West, S. Zhang, M.-Y. Chou, C.-K. Shih, Epitaxial growth of two-dimensional insulator monolayer honeycomb BeO, *ACS Nano* 15 (2021) 2497–2505, <https://doi.org/10.1021/acsnano.0c06596>.
- [9] H.L. Zhuang, R.G. Hennig, Computational identification of single-layer CdO for electronic and optical applications, *Appl. Phys. Lett.* 103 (2013), 212102, <https://doi.org/10.1063/1.4831972>.
- [10] H. Zheng, X.-B. Li, N.-K. Chen, S.-Y. Xie, W.Q. Tian, Y. Chen, H. Xia, S.B. Zhang, H.-B. Sun, Monolayer II-VI semiconductors: a first-principles prediction, *Phys. Rev. B* 92 (2015), 115307, <https://doi.org/10.1103/PhysRevB.92.115307>.
- [11] D.A. Bandurin, A.V. Tyurnina, G.L. Yu, A. Mishchenko, V. Zolyomi, S.V. Morozov, R.K. Kumar, R.V. Gorbačev, Z.R. Kudrynskyi, S. Pezzini, Z.D. Kovalyuk, U. Zeitler, K.S. Novoselov, A. Patanè, L. Eaves, I.V. Grigorieva, V.I. Fal'ko, A.K. Geim, Y. Cao, High electron mobility, quantum Hall effect and anomalous optical response in atomically thin InSe, *Nat. Nanotechnol.* 12 (2017) 223–227, <https://doi.org/10.1038/nano.2016.242>.
- [12] X.-P. Wang, X.-B. Li, N.-K. Chen, J.-H. Zhao, Q.-D. Chen, H.-B. Sun, Electric field analyses on monolayer semiconductors: the example of InSe, *Phys. Chem. Chem. Phys.* 20 (2018) 6945–6950, <https://doi.org/10.1039/C7CP07270H>.
- [13] W. Ding, J. Zhu, Z. Wang, Y. Gao, D. Xiao, Y. Gu, Z. Zhang, W. Zhu, Prediction of intrinsic two-dimensional ferroelectrics in In<sub>2</sub>Se<sub>3</sub> and other III<sub>2</sub>-VI<sub>3</sub> van der Waals materials, *Nat. Commun.* 8 (2017), 14956, <https://doi.org/10.1038/ncomms14956>.
- [14] Y.-T. Huang, N.-K. Chen, Z.-Z. Li, X.-B. Li, X.-P. Wang, Q.-D. Chen, H.-B. Sun, S. Zhang, Mexican-hat potential energy surface in two-dimensional III<sub>2</sub>-VI<sub>3</sub> materials and the importance of entropy barrier in ultrafast reversible ferroelectric phase change, *Appl. Phys. Rev.* 8 (2021), 031413, <https://doi.org/10.1063/5.0056695>.

- [15] Y. Huang, N. Chen, Z. Li, X. Wang, H. Sun, S. Zhang, X. Li, Two-dimensional in 2 Se 3 : a rising advanced material for ferroelectric data storage, *Info* (2022), <https://doi.org/10.1002/inf2.12341>.
- [16] Q.H. Wang, K. Kalantar-Zadeh, A. Kis, J.N. Coleman, M.S. Strano, Electronics and optoelectronics of two-dimensional transition metal dichalcogenides, *Nat. Nanotechnol.* 7 (2012) 699–712, <https://doi.org/10.1038/nnano.2012.193>.
- [17] H. Wang, Q. Wang, Y. Cheng, K. Li, Y. Yao, Q. Zhang, C. Dong, P. Wang, U. Schwingenschlögl, W. Yang, X.X. Zhang, Doping monolayer graphene with single atom substitutions, *Nano Lett.* 12 (2012) 141–144, <https://doi.org/10.1021/nl2031629>.
- [18] D. Wang, D. Han, X.-B. Li, N.-K. Chen, D. West, V. Meunier, S. Zhang, H.-B. Sun, Charged defects in two-dimensional semiconductors of arbitrary thickness and geometry: formulation and application to few-layer black phosphorus, *Phys. Rev. B* 96 (2017), 155424, <https://doi.org/10.1103/PhysRevB.96.155424>.
- [19] D. Wang, D. Han, X.-B. Li, S.-Y. Xie, N.-K. Chen, W.Q. Tian, D. West, H.-B. Sun, S.B. Zhang, Determination of formation and ionization energies of charged defects in two-dimensional materials, *Phys. Rev. Lett.* 114 (2015), 196801, <https://doi.org/10.1103/PhysRevLett.114.196801>.
- [20] D. Han, X.-B. Li, D. Wang, N.-K. Chen, X.-W. Fan, Doping in the two-dimensional limit: p/n -type defects in monolayer ZnO, *Phys. Rev. B* 105 (2022), 024104, <https://doi.org/10.1103/PhysRevB.105.024104>.
- [21] Dan Wang, Xian-Bin Li, Hong-Bo Sun, Native defects and substitutional impurities in two-dimensional monolayer InSe, *Nanoscale* 9 (2017) 11619–11624, <https://doi.org/10.1039/C7NR03389C>.
- [22] D. Wang, D. Han, D. West, N.-K. Chen, S.-Y. Xie, W.Q. Tian, V. Meunier, S. Zhang, X.-B. Li, Excitation to defect-bound band edge states in two-dimensional semiconductors and its effect on carrier transport, *Npj Comput Mater* 5 (2019) 8, <https://doi.org/10.1038/s41524-018-0145-0>.
- [23] A. Laref, W. Sekkal, A. Zaoui, M. Certier, H. Aourag, Tight-binding calculations of electronic properties of AgI, *J. Appl. Phys.* 86 (1999) 4435–4439, <https://doi.org/10.1063/1.371382>.
- [24] R.H. Victoria, Calculated electronic structure of silver halide crystals, *Phys. Rev. B* 56 (1997) 4417–4421, <https://doi.org/10.1103/PhysRevB.56.4417>.
- [25] A. Dashora, A. Marwal, K.R. Soni, B.L. Ahuja, Electronic properties and compton profiles of silver iodide, *Pramana - J. Phys.* 74 (2010) 1017–1027, <https://doi.org/10.1007/s12043-010-0077-9>.
- [26] B.J. Morgan, P.A. Madden, Effects of lattice polarity on interfacial space charges and defect disorder in ionically conducting AgI heterostructures, *Phys. Rev. Lett.* 107 (2011), 206102, <https://doi.org/10.1103/PhysRevLett.107.206102>.
- [27] M.C. Lucking, W. Xie, D.-H. Choe, D. West, T.-M. Lu, S.B. Zhang, Traditional semiconductors in the two-dimensional limit, *Phys. Rev. Lett.* 120 (2018), 086101, <https://doi.org/10.1103/PhysRevLett.120.086101>.
- [28] D. Wang, X.-B. Li, D. Han, W.Q. Tian, H.-B. Sun, Engineering two-dimensional electronics by semiconductor defects, *Nano Today* 16 (2017) 30–45, <https://doi.org/10.1016/j.nantod.2017.07.001>.
- [29] G. Kresse, J. Furthmüller, Efficient iterative schemes for *ab initio* total-energy calculations using a plane-wave basis set, *Phys. Rev. B* 54 (1996) 11169–11186, <https://doi.org/10.1103/PhysRevB.54.11169>.
- [30] G. Kresse, J. Furthmüller, Efficiency of ab-initio total energy calculations for metals and semiconductors using a plane-wave basis set, *Comput. Mater. Sci.* 6 (1996) 15–50, [https://doi.org/10.1016/0927-0256\(96\)00008-0](https://doi.org/10.1016/0927-0256(96)00008-0).
- [31] J.P. Perdew, K. Burke, M. Ernzerhof, Generalized gradient approximation made simple, *Phys. Rev. Lett.* 77 (1996) 3865–3868, <https://doi.org/10.1103/PhysRevLett.77.3865>.
- [32] G. Kresse, D. Joubert, From ultrasoft pseudopotentials to the projector augmented-wave method, *Phys. Rev. B* 59 (1999) 1758–1775, <https://doi.org/10.1103/PhysRevB.59.1758>.
- [33] S. Nosé, A unified formulation of the constant temperature molecular dynamics methods, *J. Chem. Phys.* 81 (1984) 511–519, <https://doi.org/10.1063/1.447334>.
- [34] A. Togo, I. Tanaka, First principles phonon calculations in materials science, *Scripta Mater.* 108 (2015) 1–5, <https://doi.org/10.1016/j.scriptamat.2015.07.021>.
- [35] S. Grimme, J. Antony, S. Ehrlich, H. Krieg, A consistent and accurate *ab initio* parametrization of density functional dispersion correction (DFT-D) for the 94 elements H–Pu, *J. Chem. Phys.* 132 (2010), 154104, <https://doi.org/10.1063/1.3382344>.
- [36] S. Zhang, J. Northrup, Chemical potential dependence of defect formation energies in GaAs: application to Ga self-diffusion, *Phys. Rev. Lett.* 67 (1991) 2339–2342, <https://doi.org/10.1103/PhysRevLett.67.2339>.
- [37] D. Han, D. West, X.-B. Li, S.-Y. Xie, H.-B. Sun, S.B. Zhang, Impurity doping in SiO<sub>2</sub>: formation energies and defect levels from first-principles calculations, *Phys. Rev. B* 82 (2010), 155132, <https://doi.org/10.1103/PhysRevB.82.155132>.
- [38] H.-P. Komsa, A. Pasquarello, Finite-size supercell correction for charged defects at surfaces and interfaces, *Phys. Rev. Lett.* 110 (2013), 095505, <https://doi.org/10.1103/PhysRevLett.110.095505>.
- [39] R.B. Wilsey, LIII. The crystalline structures of silver iodide, *Philosophical Magazine Series* 46 (6) (1923) 487–496, <https://doi.org/10.1080/14786442308634272>.
- [40] A. Jain, S.P. Ong, G. Hautier, W. Chen, W.D. Richards, S. Dacek, S. Cholia, D. Gunter, D. Skinner, G. Ceder, K.A. Persson, Commentary: the Materials Project: a materials genome approach to accelerating materials innovation, *Apl. Mater.* 1 (2013), 011002, <https://doi.org/10.1063/1.4812323>.
- [41] G.D. Watkins, Negative-U properties for defects in solids, in: P. Grosse (Ed.), *Advances in Solid State Physics*, Springer Berlin Heidelberg, 1984, pp. 163–189, <https://doi.org/10.1007/BFb0107450>.
- [42] A.V. Krukau, O.A. Vydrov, A.F. Izmaylov, C.E. Scuseria, Influence of the exchange screening parameter on the performance of screened hybrid functionals, *J. Chem. Phys.* 125 (2006), 224106, <https://doi.org/10.1063/1.2404663>.
- [43] J. Ma, Z.G. Yu, Y.-W. Zhang, Tuning deep dopants to shallow ones in 2D semiconductors by substrate screening: the case of X S (X = Cl, Br, I) in MoS<sub>2</sub>, *Phys. Rev. B* 95 (2017), 165447, <https://doi.org/10.1103/PhysRevB.95.165447>.
- [44] D. Wang, R. Sundararaman, Substrate effects on charged defects in two-dimensional materials, *Phys. Rev. Mater.* 3 (2019), 083803, <https://doi.org/10.1103/PhysRevMaterials.3.083803>.
- [45] D. Wang, R. Sundararaman, Layer dependence of defect charge transition levels in two-dimensional materials, *Phys. Rev. B* 101 (2020), 054103, <https://doi.org/10.1103/PhysRevB.101.054103>.
- [46] D. Wang, X.-B. Li, H.-B. Sun, Modulation doping: a strategy for 2D materials electronics, *Nano Lett.* 21 (2021) 6298–6303, <https://doi.org/10.1021/acs.nanolett.1c02192>.
- [47] B. Cai, S. Zhang, Z. Yan, H. Zeng, Noncovalent molecular doping of two-dimensional materials, *ChemNanoMat* 1 (2015) 542–557, <https://doi.org/10.1002/cnma.201500102>.
- [48] B. Mortazavi, M. Silani, E.V. Podryabinkin, T. Rabczuk, X. Zhuang, A.V. Shapeev, First-principles multiscale modeling of mechanical properties in graphene/borophene heterostructures empowered by machine-learning interatomic potentials, *Adv. Mater.* 33 (2021), 2102807, <https://doi.org/10.1002/adma.202102807>.
- [49] B. Mortazavi, B. Javvaji, F. Shojaei, T. Rabczuk, A.V. Shapeev, X. Zhuang, Exceptional piezoelectricity, high thermal conductivity and stiffness and promising photocatalysis in two-dimensional MoSi<sub>2</sub>N<sub>4</sub> family confirmed by first-principles, *Nano Energy* 82 (2021), 105716, <https://doi.org/10.1016/j.nanoen.2020.105716>.
- [50] B. Andryushechkin, T. Pavlova, Adsorption of molecular iodine on the Ag(111) surface: phase transitions, silver reconstruction, and iodide growth, *J. Chem. Phys.* 156 (2022), 164702, <https://doi.org/10.1063/5.0089915>.
- [51] K. Mustonen, C. Hofer, P. Kotrusz, A. Markevich, M. Hulman, C. Mangler, T. Susi, T.J. Pennycook, K. Hricovini, C. Richter, J.C. Meyer, J. Kotakoski, V. Skákalová, Toward exotic layered materials: 2D cuprous iodide, *Adv. Mater.* 34 (2022), 2106922, <https://doi.org/10.1002/adma.202106922>.
- [52] M.-Y. Ma, D. Han, N.-K. Chen, D. Wang, X.-B. Li, Recent progress in double-layer honeycomb structure: a new type of two-dimensional material, *Materials* 15 (2022) 7715, <https://doi.org/10.3390/ma15217715>.